Electronic Supplementary Material (ESI) for Journal of Materials Chemistry A.

Electronic perturbation by interfacial coupling of the iridium cluster and Cu_3P accelerates water splitting kinetics

Payam Ahmadian Koudakan[a], Xiaobin Hao[b], Amirabbas Mosallanezhad[a], Cong Wei[a], Jinyan Cai[a], Junxin Xiao[a], Yuqing Yang[b], Bo Liu[a], Jun Liu*[c],Yanyan Fang*[a], Gongming Wang*[a]

[a]Hefei National Laboratory for Physical Science at the Microscale, Department of Applied Chemistry, University of Science and Technology of China, Hefei, Anhui 230026, China.

[b]School of Materials and Chemical Engineering, Chuzhou University, Chuzhou, Anhui 239000, China.

[c]Institute of Solid State Physics, Hefei Institutes of Physical Science, Chinese Academy of Sciences, Hefei 230031, China.

*Corresponding authors E-mail: jliu@issp.ac.cn; fr1478@mail.ustc.edu.cn; wanggm@ustc.edu.cn.

1. Computational details:

DFT calculation was performed using the CASTEP program as implemented in the Materials Studios package of Accelrys Inc. [1] The exchange-correlation potential is described through the generalized gradient approximation proposed by Perdew, Burke, and Ernzerhof (GGA-PBE). [2,3] The cutoff energy for the plane wave was set to 400 eV. The energy criterion was set to 5×10^{-6} eV in the iterative solution of the Kohn-Sham equation. We choose $Cu_3P(300)$ surface, which was identified by the high-resolution TEM technique, to represent the synthesized Cu_3P catalyst. The surface slab is a $p(2\times2)$ supercell with three layers and the vacuum thickness between slabs in the z direction is set to 20 Å. To model the $Ir_{CL}@Cu_3P$ catalyst, the Ir cluster (including 24 Ir atoms) is constructed on the $Cu_3P(300)$ surface (figure S14a) based on the experimental characterization. The Ir and Pt catalysts were modeled by Ir(111) and Pt(111) surfaces (figure S14b and c), which were the most preferred exposed facet in general. The two surfaces are the four-layer slabs with the $p(3\times3)$ supercell and vacuum thickness of 15 Å. It is noted all catalyst models can allow sufficient distance between periodic images so that lateral interactions are minimized. The sampling of the Brillouin zone was performed with a 3×3×1 Monkhorst−Pack k-point mesh [4]. The force convergence criterion on the atoms was set to 0.03 eV $Å^{-1}$. The barriers and reaction energies for H_2O dissociation to OH and H on different catalyst models were calculated using linear synchronous transitions (LST) and quadratic synchronous transitions (QST) methods.[5] The free energy of hydrogen adsorption ΔG_{H^*} at T=300 K is further calculated from $\Delta G_{H^*} = E_{slab+H} - E_{slab} - 0.5*E_{H2} + 0.24$ eV, where the value of 0.24 eV represents the correction of zero-point energy and entropy of hydrogen state. [6] The following equations were used to calculate the fractional d-band filling (f_d), d-band center (ε_d), and d-band width (W_d) [7]:

$$f_d = \frac{\int_{-\infty}^{E_f} \rho.dE}{\int_{-\infty}^{\infty} \rho.dE}$$

$$\varepsilon_d = \frac{\int_{-\infty}^{E_f} \rho.E.dE}{\int_{-\infty}^{E_f} \rho.dE}$$

$$W_d^2 = \frac{\int_{-\infty}^{E_f} \rho.E^2.dE}{\int_{-\infty}^{E_f} \rho.dE}$$

where, ρ, E and E_f are the density of electronic state per volume, energy of the electron and Fermi energy, respectively.

2. Figures:

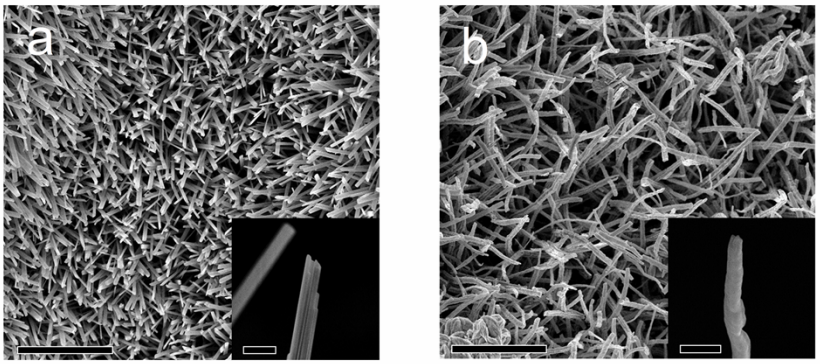

Figure S1. The Low magnification SEM images of (a) $Cu(OH)_2$ and (b) Cu_3P (scale bar: 5 μm); and inset: the high magnification SEM image of (a) $Cu(OH)_2$ and (b) Cu_3P nanowire (scale bar: 500 nm).

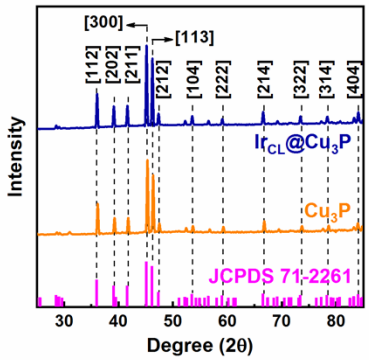

Figure S2. XRD of the Cu_3P and $Ir_{CL}@Cu_3P$ samples.

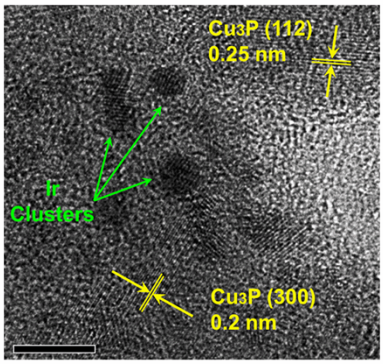

Figure S3. The low magnification HR-TEM image of $Ir_{CL}@Cu_3P$ (scale bar: 5 nm).

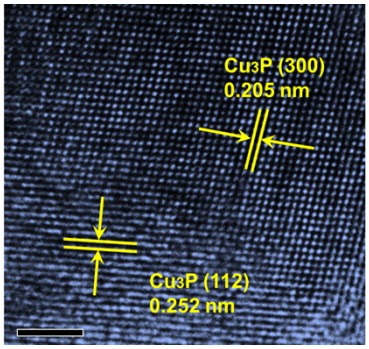

Figure S4. The HR-TEM image of Cu_3P (scale bar: 2 nm).

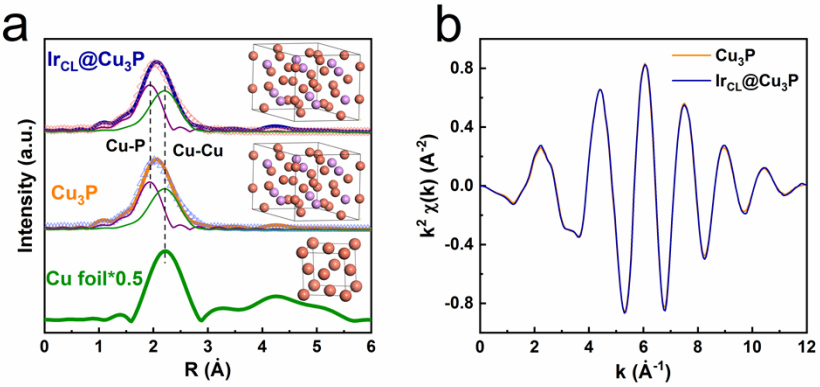

Figure S5: (a) Best fitting and experimental data of Cu K-edge k^3-weighted EXAFS of Cu_3P, $Ir_{CL}@Cu_3P$, and Co foil in R-space. (b) The Cu K-edge k^3-weighted EXAFS in k-space for Cu_3P, $Ir_{CL}@Cu_3P$.

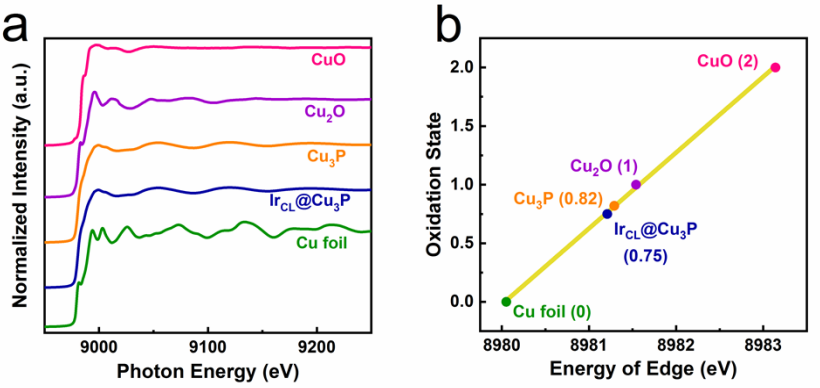

Figure S6. (a) Normalized Cu K-edge XANES spectra of Cu_3P, $Ir_{CL}@Cu_3P$, CuO, Cu_2O, and Cu foil. (b) Linear fitting of average oxidation state toward energy of Cu K-edge.

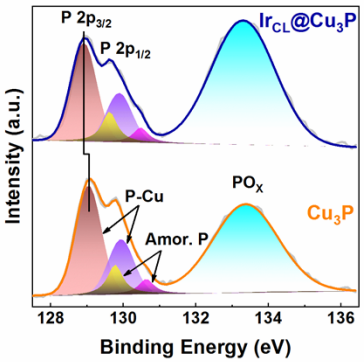

Figure S7. The high-resolution XPS spectra of P 2p for the Cu_3P and $Ir_{CL}@Cu_3P$ samples.

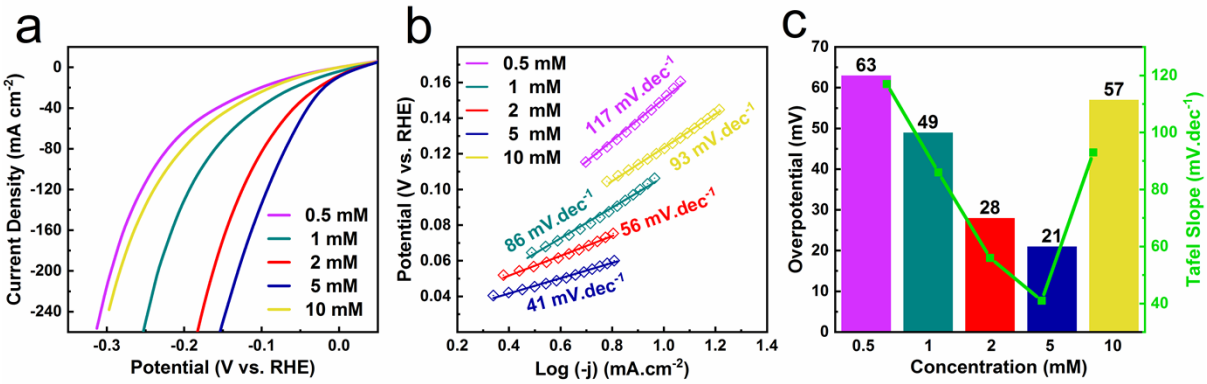

Figure S8. (a) The LSV curves (b) Tafel plot and (c) comparison between $Ir_{CL}@Cu_3P$ samples with different concentration of iridium solution.

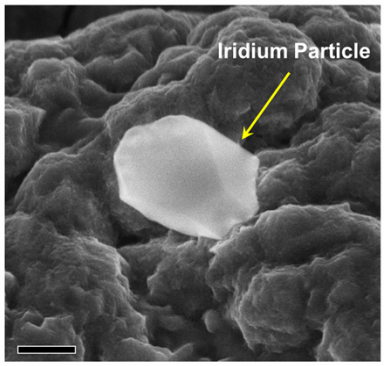

Figure S9. The SEM image of $Ir_{CL}@Cu_3P$ prepared with 10 mM iridium solution (scale bar: 300 nm).

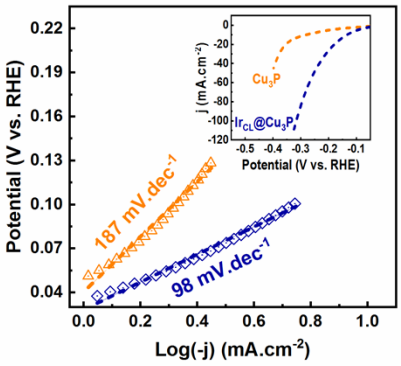

Figure S10. Tafel plot and (inset: corresponding polarization curves) of $Ir_{CL}@Cu_3P$ in 1M KOD.

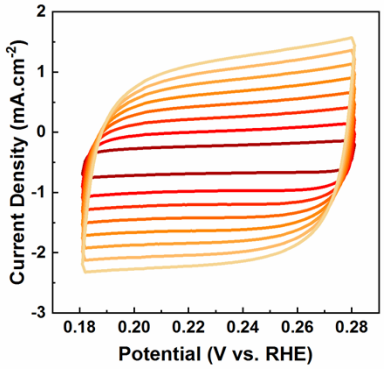

Figure S11. Non-faradic cyclic voltammetry curves of Cu_3P in 1 M KOH.

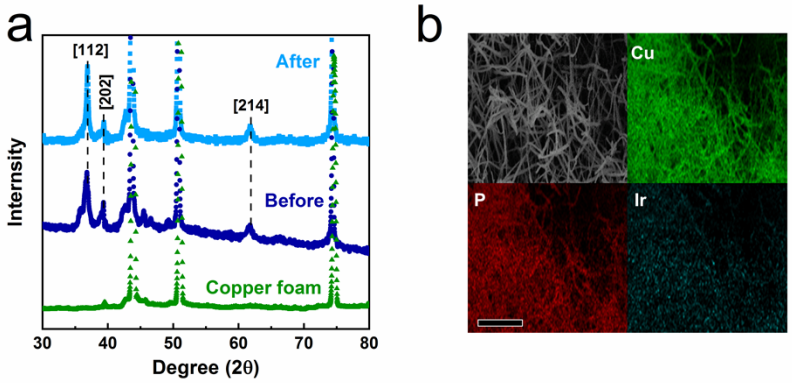

Figure S12. (a) XRD patterns of $Ir_{CL}@Cu_3P$ before and after stability test (scale bar: 5 μm). (b) SEM and corresponding elemental mapping of $Ir_{CL}@Cu_3P$ after stability test.

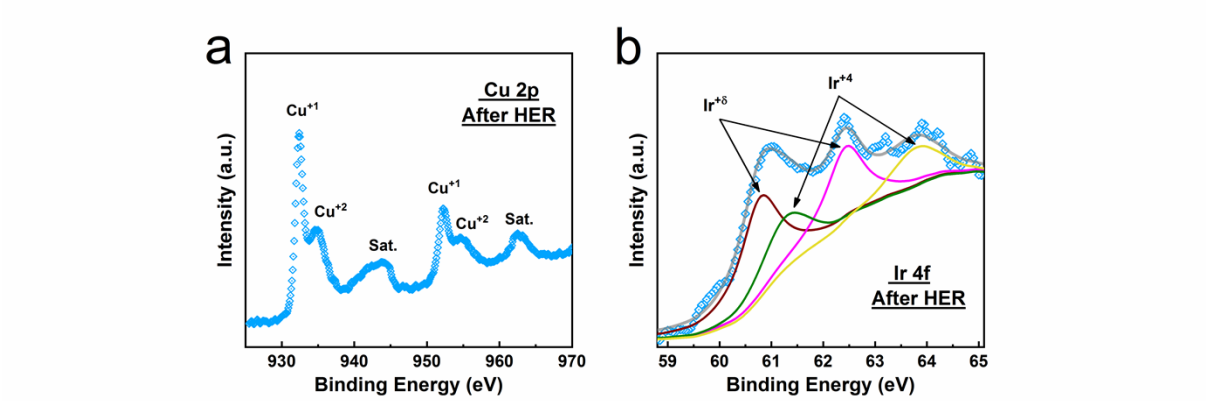

Figure S13. XPS spectra of (a) Cu 2p and (b) Ir 4f of Ir_{CL}@Cu_3P after stability test.

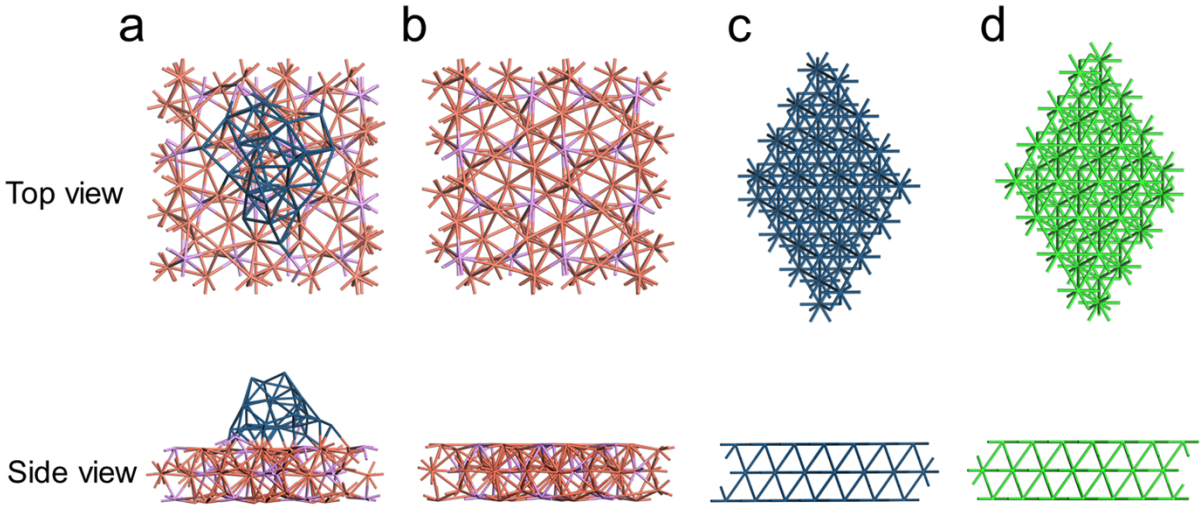

Figure S14. Side and top views of (a) Ir_{CL}@Cu_3P, (b) Cu_3P(300), (c) Ir(111), and (d) Pt(111) models.

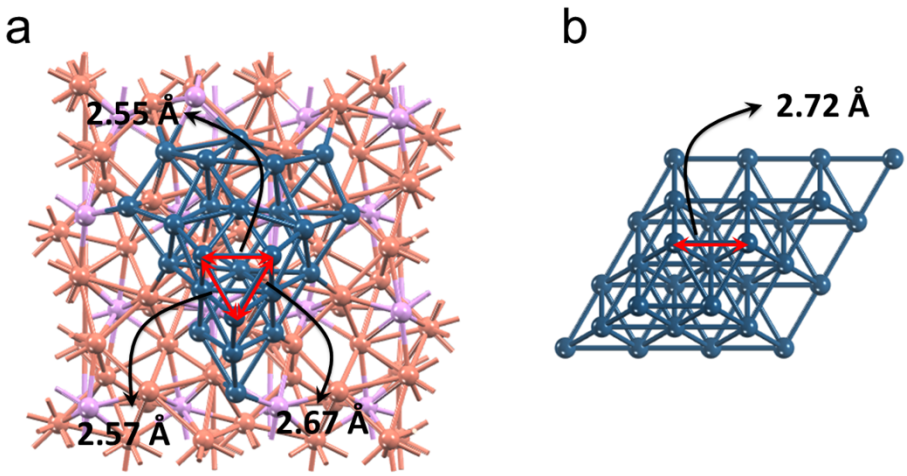

Figure S15. The Ir-Ir bond distance in relaxed surfaces of (a) $Ir_{CL}@Cu_3P$ and (b) Ir(111) models.

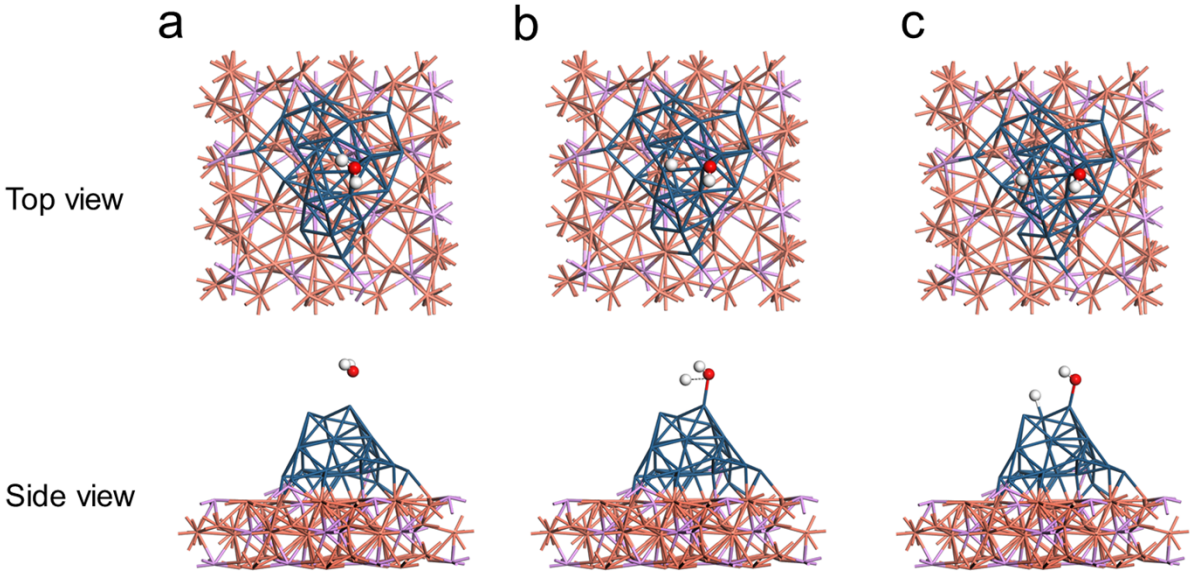

Figure S16. The top and side views for configurations of H_2O dissociation on $Ir_{CL}@Cu_3P$. (a) Initial state; (b) Transition state; (c) Final state.

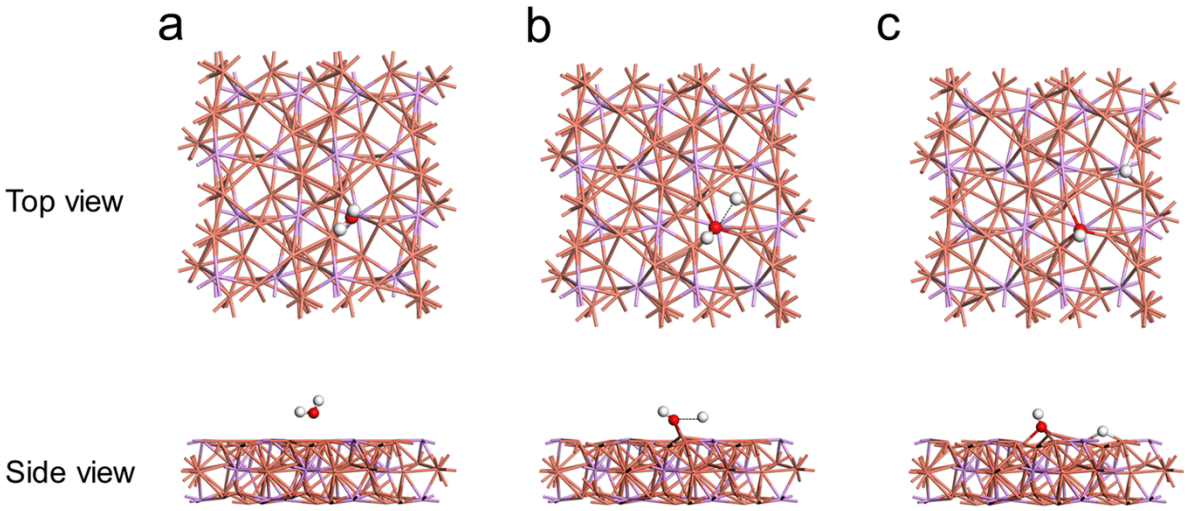

Figure S17. The top and side views for configurations of H_2O dissociation on $Cu_3P(300)$. (a) Initial state; (b) Transition state; (c) Final state.

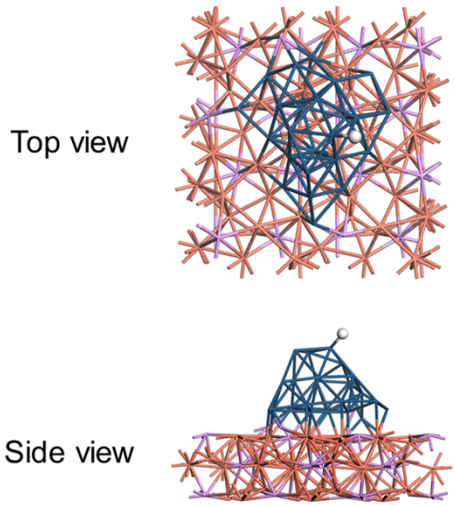

Figure S18. The top and side views of H adsorption on $Ir_{CL}@Cu_3P$ catalyst.

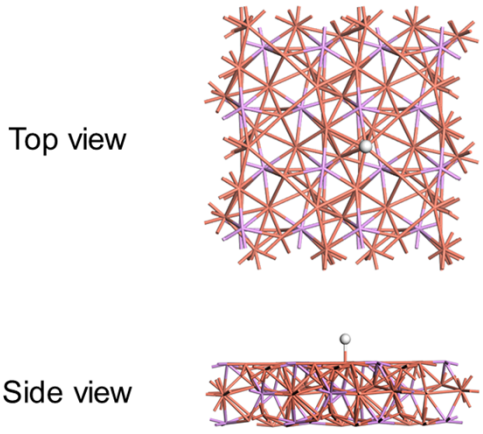

Figure S19. The top and side views of H adsorption on $Cu_3P(300)$ surface.

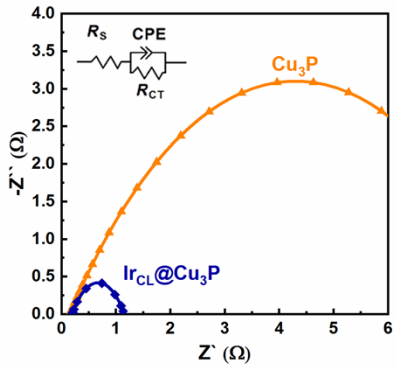

Figure S20. Electrochemical impedance spectroscopy of Cu_3P, and $Ir_{CL}@Cu_3P$ measured at 1.37 V vs. RHE.

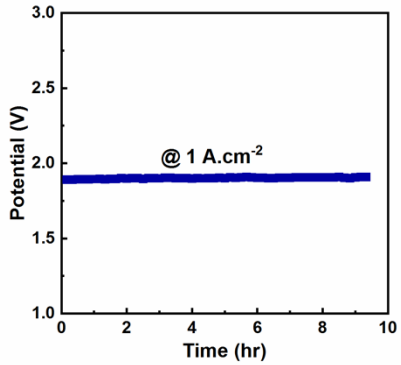

Figure S21. The amperometric current-time curve of $Ir_{CL}@Cu_3P$ || $Ir_{CL}@Cu_3P$ full cell

3. Tables:

Table S1. Fitting parameters of Ir L_3-edge and Cu K-edge scattering path for the Ir_{CL}@Cu_3P and Cu_3P samples.

Sample	Test	Shell	R (Å) [a]	N [b]	δ^2 (Å) [c]	ΔE_0 [d]	R-factor [e]
Ir_{CL}@Cu_3P	Ir L_3-edge	Ir-Ir	2.55	7.4	0.0031	5.338	0.0050
	Cu K-edge	Cu-Cu	2.21	5.2	0.0167	4.079	0.0068
		Cu-P	1.93	2.0	0.0070		
Cu_3P	Cu K-edge	Cu-Cu	2.21	5.0	0.0165	3.943	0.0057
		Cu-P	1.93	2.0	0.0070		
Ir foil	Ir L_3-edge	Ir-Ir	2.70	12	0.0024	7.919	0.0027
Cu foil	Cu K-edge	Cu-Cu	2.21	12	0.0084	4.812	0.0016

a: bond length; b: coordination number; c: Debye-Waller factors; d: the inner potential correction: e: goodness of fitting.

Table S2. Comparison of OWS catalysts using AEMWE.

Catalyst		Loading Mass (mg/cm^{-2})		Electrolyte	E_{cell} (V)	Ref.
Anode	Cathode	Anode	Cathode			
Ir_{CL}@Cu_3P	Ir_{CL}@Cu_3P	8.7	8.7	1 M KOH	1.94	This Work
IrO_2	Pt black	3	3	H_2O	1.9	*Chem. Mater.* **2014**, 26, 5675−5682.
Ir black	Pt/C	2.7	2.7	H_2O	1.9	*Joule* **2021**, 5, 1776−1799.
$Ni_{0.75}Fe_{2.25}O_4$	Pt/C	1	1	1 M KOH	1.9	*Chem Eng J.* **2020**, 420, 127670.

Co_3O_4/rGO	NiCo/rGO	1	1	1 M KOH	1.9	*Renewable Energy.* **2020**, 154, 1122-1131.
NiFe	NiFe	20	20	1 M KOH	1.93	*Energy. Sci. Technol.* **2021**, 14, 6338−6348.
$NiCo_2O_4$	$Fe_{60}Co_{20}Si_{10}B_{10}$	5	5	10% KOH	2	*Electrochim Acta.* **2019**, 306, 688-697.
Co NPs	PtNi NWs	0.4	0.1	1 M KOH	2	*ACS Catal.* **2020**, 10, 9953-9966.
$NiCo_2O_4$	$NiCo_2O_4$	2	2	1 M KOH	2	*J Mater Chem A.* **2020**, 8, 17089-17097.
$Cu_{0.81}Co_{2.19}O_4$	Co_3S_4	-	-	1 M KOH	2	*Int J Hydrogen Energy.* **2020**, 45, 36-45.
Ir black	NiCu alloy	3	5	1 M KOH	2	*Electrochim Acta.* **2021**, 371, 137837.
$Ni_{0.7}Co_{0.3}O_X$	Pt/C	2	1	1 wt% $KHCO_3$	2.03	*RSC Adv.* **2016**, 6, 90397−90400.
$CuCoO_X$	Ni/(CeO_2-La_2O_3)/C	30	7.4	1 wt% $KHCO_3$	2.05	*Int. J. Hydrog. Energy* **2017**, 42, 10752−10761.
NiAl	NiAlMo	47.9	42.7	1 M KOH	2.05	*ACS Appl. Energy Mater.* **2019**, 2, 7903−7912.
$NiFeO_X$	NiFeCo	5	5	1 M KOH	2.09	*RSC Adv*. **2020**, 10, 37429−37438.
Ir-Ni/Mo_5N_6	Ir-Ni/Mo_5N_6	2.5	2.5	1 M KOH	2.1	*J. Colloid Interface Sci.* **2022**, 628, 306-3014.
IrO_2	Pt/C	0.6	0.3	H_2O	2.1	*ACS Appl. Mater*. **2019**, 11, 9696−9701.
NiFeCo	Ni mesh	7	n/a	4 M NaOH	2.2	*Int J Hydrogen Energy* **2020**, 45, 24232-24247.
CuCoO	Ni thin film	0.18	0.4	1 M KOH	2.2	*J Power Sources.* **2019**, 415, 136-144.
Ni foam	Ni foam	n/a	n/a	1.95 M KOH	2.26	*Electrochim. Acta* **2017**, 248, 547−555.
Ni-Co	Ni foam	0.75	n/a	0.5 M KOH	2.29	*Mater Chem Phys.* **2020**, 242, 122537.
$NiCoFeO_X$	Pt/C	3	3	H_2O	2.3	*ACS Catal.* **2019**, 9, 7-15.
IrO_3	Ni-Co-S	-	-	1 M KOH	2.4	*Int J Energy Res.* **2021**, 45, 1918-1931.

4. References:

[1] Clark, S. J. et al. First principles methods using CASTEP. Z. fuer Krist. 2005, **220**, 567–570.

[2] Perdew, J. P.; Burke, K.; Ernzerhof, M. Generalized Gradient Approximation Made Simple. *Phys. Rev. Lett.* 1996, **77**, 3865−3868.

[3] White, J. A.; Bird, D. M. Implementation of Gradient-Corrected Exchange-Correlation Potentials in Car-Parrinello Total-Energy Calculations. *Phys. Rev. B: Condens. Matter Mater. Phys.* 1994, **50**, 4954−4957.

[4+1] Sato, S. A. Two-step Brillouin zone sampling for efficient computation of electron dynamics in solids. *J. Phys.: Condens. Matter.* 2022, **34**, 095903.

[5] Henkelman, G.; Jonsson, H. Improved tangent estimate in the nudged elastic band method for finding minimum energy paths and saddle points. *J. Chem. Phys.* 2000, **113**, 9978−9985.

[6] Monkhorst, H. J.; Pack J. D. Special points for Brillouin-zone integrations. *Phys. Rev. B.* 1976, **13**, 5188.

[7] Seifitokaldani, A.; Savadogo, O.; Perrier, M. Density Functional Theory (DFT) Computation of the Oxygen Reduction Reaction (ORR) on Titanium Nitride (TiN) Surface. Electrochim. Acta. 2014, **141**, 25-32.